Communications in Nonlinear Science and Numerical Simulation 121 (2023) 107193

Contents lists available at ScienceDirect

Communications in Nonlinear Science and Numerical Simulation

journal homepage: www.elsevier.com/locate/cnsns

Research paper

Semi-analytical method to study piecewise linear oscillators

Agustín Hernández Rocha [a], Damián H. Zanette [a,b], Marian Wiercigroch [c,*]

[a] Centro Atómico Bariloche and Instituto Balseiro, Comisión Nacional de Energía Atómica and Universidad Nacional de Cuyo, 8400 San Carlos de Bariloche, Río Negro, Argentina
[b] Consejo Nacional de Investigaciones Científicas y Técnicas, Argentina
[c] Centre for Applied Dynamics Research, School of Engineering, University of Aberdeen, Aberdeen, AB24 3UE, Scotland, United Kingdom

ARTICLE INFO

Article history:
Received 12 August 2022
Received in revised form 16 February 2023
Accepted 21 February 2023
Available online 27 February 2023

Keywords:
Piecewise linear oscillator
Semi-analytical solution
Numerical simulation
Nonlinear dynamics analysis

ABSTRACT

This article proposes a semi-analytical method to investigate the dynamics and bifurcation scenarios of piecewise linear oscillators. The method is based on a mapping technique with a matrix structure that allows easy and rapid construction of any periodic orbit. When validated against direct numerical integration simulations, a good correlation and an accurate prediction of bifurcation phenomena were shown. The method is applied to analyse the nonlinear dynamic responses and bifurcations scenarios causes by changes of stiffness and viscous damping. A set of minimum conditions that the system must meet to present period doubling bifurcations and sub-harmonic orbits was given.

1. Introduction

Piecewise-smooth dynamical systems are essential to the study of engineering devices which include mechanisms that produce sudden changes in behaviour. Among them, piecewise linear systems are the simplest and most widely used non-smooth models. Practical applications of these models include electrical circuits with switches, diodes or transistors [1], mechanical systems with motion limiting constraints [2], assemblies with impact between parts [3], slip and friction problems [4,5], and control systems that use switching-based logics [6]. For mechanical systems, examples of how impact oscillators can be used to analyse their dynamics can be found in studies of gear assemblies [7–9], heat-exchanger dynamics [10,11], and percussive drilling performance [12,13]. Sudden changes in the parameters that control these systems induces rich and complex behaviour. Their strong inherent nonlinearity makes chaotic dynamics become frequent. Collisions also lead to wear of the components of the system. Determination of the response allows preventing unwanted wear or improper functioning, and provides important information useful for mechanical design. Recent contributions to fundamental and applied nonlinear dynamics of impact oscillators have been done through analytical and numerical investigations [14,15], design of nonlinear controllers [16,17], energy harvesting and vibration transmission [18–20], design of experimental rigs [21] and nonlinear resonances [22,23].

Particularly, in nuclear power plants there are several components whose dynamics can by modelled using piecewise linear systems. Flow-induced vibrations of fuel assemblies, heat exchangers, and steam generators are important structural problems where these models have been applied [24–26]. Using these non-smooth systems, the chaotic dynamics of heat exchanger tubes impacting on the generally loose baffle plates was first analysed by Paidoussis [11]. The dynamics of heat

* Corresponding author.
E-mail address: m.wiercigroch@abdn.ac.uk (M. Wiercigroch).

https://doi.org/10.1016/j.cnsns.2023.107193

exchangers and related wear phenomena in spacer-tube zones was investigated by Goyder et al. [10], using dimensional analysis, physical modelling involving piecewise linear approach and numerical simulations. Computation of nonlinear vibro-impact responses of loosely supported heat-exchanger tubes subjected to fluidelastic coupling forces, as well as validation against experimental results, has been presented by Piteau et al. [27]. A piecewise linear system has been used as well by Christon et al. [28] to model fuel structures implicit large-eddy CFD simulations, presenting a new approach to estimate fuel rod wear in grid-to-rad fretting problems. These few examples reveal how piecewise linear systems have become important models for studying dynamics of various engineering systems.

To understand the multiple phenomena involved in non-smooth linear systems, analytical and numerical methods have been developed. Shaw and Holmes [9] presented a detailed description of a classical base-excited piecewise linear system with a discontinuity in the restoring force. The limiting case in which stiffness slope approaches infinity, representing a rigid impact oscillator, was also considered. A general procedure to analyse stability of these non-smooth systems was shown by Natsiavas [29], where different bifurcation scenarios were disclosed, and the impossibility of having Hopf bifurcations with positive damping was demonstrated. An impact condition was modelled introducing a constant of restitution factor (COR) by Foale [30], also inducing critical phenomena and multistability. In turn, Chin et al. [31] studied bifurcations in impact oscillators using the Nordmark map [32] as an equivalent discrete model.

The oscillator with a play was studied simultaneously by Li et al. [33] and Kleczka et al. [34]. In these studies, the impact condition was introduced with a COR and a linear stiffness definition, respectively. The latter contribution showed how this kind of systems is characterized by sudden changes of chaotic dynamics, named crises, and demonstrated how their occurrence can be determined numerically. Later, Wiercigroch [35,36] provided a further overview of the system dynamics through codimension-1 bifurcation scenarios, and showed experimental evidence on bifurcation scenarios and chaotic motion. The nature of periodic and chaotic orbits of similar systems were comprehensively studied by Luo and his co-workers, e.g. [37], where predictions on stable and unstable orbits based on mapping structures were presented in [38]. These authors were the first to apply analytical methods based on maps to investigate the global dynamics of piecewise smooth systems. In the following years such methods were used to study other types of piecewise linear oscillators, e.g. [39–41]. Exact solutions for an oscillator with a symmetrical trilinear spring and subjected to harmonic excitation was presented by Natsiavas [42], where period-one and sub-harmonic orbits were investigated. Chong et al. [43] presented a detailed description of a piecewise linear oscillator with a play where rich and diverse dynamics of this system was investigated by numerical simulation for a wide range of system parameters.

Piecewise linear systems topic that have been extensively studied and has led to discovering of new type of bifurcations, so-called grazing bifurcations. Nordmark [32] investigated the singularities caused by grazing impact and the possibility of having non-periodic orbits beyond bifurcation. Foale [30] presented different bifurcation scenarios that can be reached in a rigid impact oscillator. A comparison between bifurcation events obtained for a rigid impact and a Hertz contact model was provided by Foale and Bishop [44]. Analytical and experimental investigations on bifurcation scenarios for an impact oscillator with a one-sided elastic constraint near grazing were presented by Ing et al. [45,46].

Dynamics near grazing is thought to be governed by a complex interplay between smooth and non-smooth bifurcations. Their relationship was studied by Mason et al. [47] and Jiang et al. [48]. Molenaar et al. [49] derived grazing impact mappings caused by rigid and elastic restraints, and concluded that the square-root singularity persists in systems with rigid restraints, whereas a 3/2 singularity is involved in those with elastic restraints. Di Bernardo et al. [50] presented a classification of main border collision bifurcation scenarios in piecewise smooth dynamical systems, summarizing and updating Feigin's original work, e.g. [51,52]. The border collision bifurcation term had been first introduced for maps by Nusse and Yorke in [53]. Also, di Bernardo et al. [54] contributed to the understanding and unification theory for non-smooth systems, by proposing general techniques for analysing bifurcations that are unique to non-smooth dynamical systems and so-called discontinuity-induced bifurcations. Jiang et al. [55] investigated the grazing-induced bifurcations in impact oscillators with one-sided elastic and with rigid constraints. Similarity between first grazing-induced bifurcation and hysteresis phenomena of bifurcation diagrams for both oscillators were shown, but some differences in the shape and evolution of the diagrams were pointed out.

The aim of this paper is to propose a systematic method, based on a mapping technique, capable of reproducing the dynamics and bifurcation behaviour in multiple configurations of an impact oscillator. A generic and versatile piecewise linear model is defined which, by variation of its parameters, comprises a wide range of practical cases. Validation of our method against numerical results is presented, for some selected parameter sets. A study of how the stiffness and damping affect the system response is also provided. Results on the relation between grazing bifurcations and chaotic dynamics are discussed.

The organization of the paper is as follows. In Section 2, the physical model is introduced. Definitions of maps and stability analysis are presented in Section 3. In Section 3.1 the six local maps for the system are defined. In Sections 3.2 and 3.3, our semi-analytical method is applied to the case of period-1 orbits, and its generalization to other kinds of orbits is described. In Section 4, a sample case of the results obtained with the semi-analytical method and a validation against numerical results are presented. The effects of modifying stiffness and damping functions are analysed in Sections 5 and 6, respectively. Section 7 is devoted to discussion and conclusions.

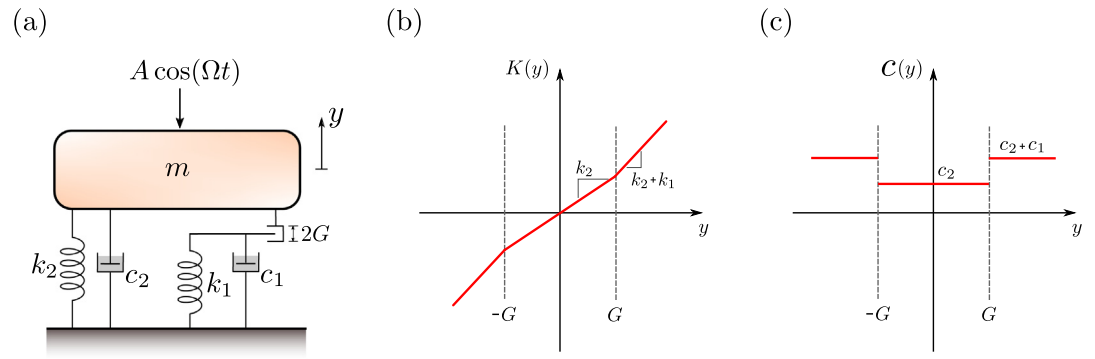

Fig. 1. (a) Physical model; (b) piecewise stiffness; (c) piecewise constant viscous damping. The coefficients k_2 and c_2 represent the intrinsic stiffness and viscous damping of the system, present over the whole range of motion. The coefficients k_1 and c_1 model the change in stiffness and damping when the oscillator impacts and crosses the discontinuity boundaries at $y = \pm G$.

2. Mathematical modelling

For the sake of brevity and clarity, we present our method by considering a low-dimensional mechanical system, within the same class of models previously studied by means of numerical and analytical techniques (e.g. [37,42,43]). Our physical model is depicted in Fig. 1(a). It is a periodically excited single degree-of-freedom oscillator with the piecewise linear restoring force presented in Fig. 1(b). The damping coefficient is piecewise constant and discontinuous, as shown in Fig. 1(c). The oscillator is excited by a harmonic external force of amplitude A and frequency Ω. The piecewise nature of both stiffness and damping makes it possible to represent diverse impact scenarios. In non-dimensional form, the equation of motion for the oscillator can be written as

$$\ddot{x} + c(x)\dot{x} + k(x) = a\cos(\omega\tau), \tag{1}$$

where $x = y/y_0$ is the dimensionless displacement, $\tau = \omega_n t$ is the dimensionless time, a is the non-dimensional forcing amplitude and ω is the non-dimensional forcing frequency, cf. [43,46,55]. The stiffness and damping functions are given by

$$k(x) = \begin{cases} (x-e) + \beta e & x > e, \\ \beta x & |x| \le e, \\ (x+e) - \beta e & x < -e, \end{cases} \tag{2}$$

$$c(x) = \begin{cases} 2\xi & x > e, \\ 2\alpha\xi & |x| \le e, \\ 2\xi & x < -e. \end{cases} \tag{3}$$

Non-dimensional parameters have been defined using arbitrary reference parameters of the displacement y_0 (here, $y_0 = G$) and the natural frequency $\omega_n = \sqrt{k_s/m}$:

$$\begin{aligned} k_s &= k_1 + k_2; \quad c_s = c_1 + c_2; \quad \xi = \tfrac{c_s}{2m\omega_n}; \quad \omega = \tfrac{\Omega}{\omega_n}; \\ a &= \tfrac{A}{y_0 k_s}; \quad \beta = \tfrac{k_2}{k_s}; \quad e = \tfrac{G}{y_0}; \quad \alpha = \tfrac{c_2}{c_s}; \end{aligned} \tag{4}$$

where ξ is the damping ratio, e is the non-dimensional gap, β is the stiffness coefficient ratio, and α the damping coefficient ratio. Impacts occur when the trajectory crosses the gap boundaries $x = \pm e$.

The rich dynamics associated with this kind of systems was previously reported in [43]. Direct numerical simulations performed by using the computational suite of numerical codes for non-smooth systems ABESPOL [56], were presented for a wide range of parameters. One of the bifurcation diagrams computed in [43] is reproduced by our own brute force numerical simulations in Fig. 2. The details about how the numerical simulations were performed are given in Section 4. For these calculations the forcing frequency ω is varied from 0.01 to 1.10, and the vertical axis corresponds to the maximum displacement (x_{max}) for each period of the external force ($T = 2\pi\omega^{-1}$). Other parameters are fixed to $\xi = 0.02$, $a = 0.3$, $\beta = 0$, $\alpha = 1$. At lower forcing frequencies, $\omega \in (0.01, 0.3414)$, the system exhibits a mixture of chaotic and periodic trajectories, with different kinds of impact orbits and diverse periodicity. Then a pitchfork bifurcation takes place at $\omega = 0.3784$ and a symmetric period-1 solution is observed up to $\omega = 0.9210$, where a saddle–node bifurcation occurs and the system jumps to a non-symmetric attractor. Additional panels of Fig. 2 show trajectories in phase space

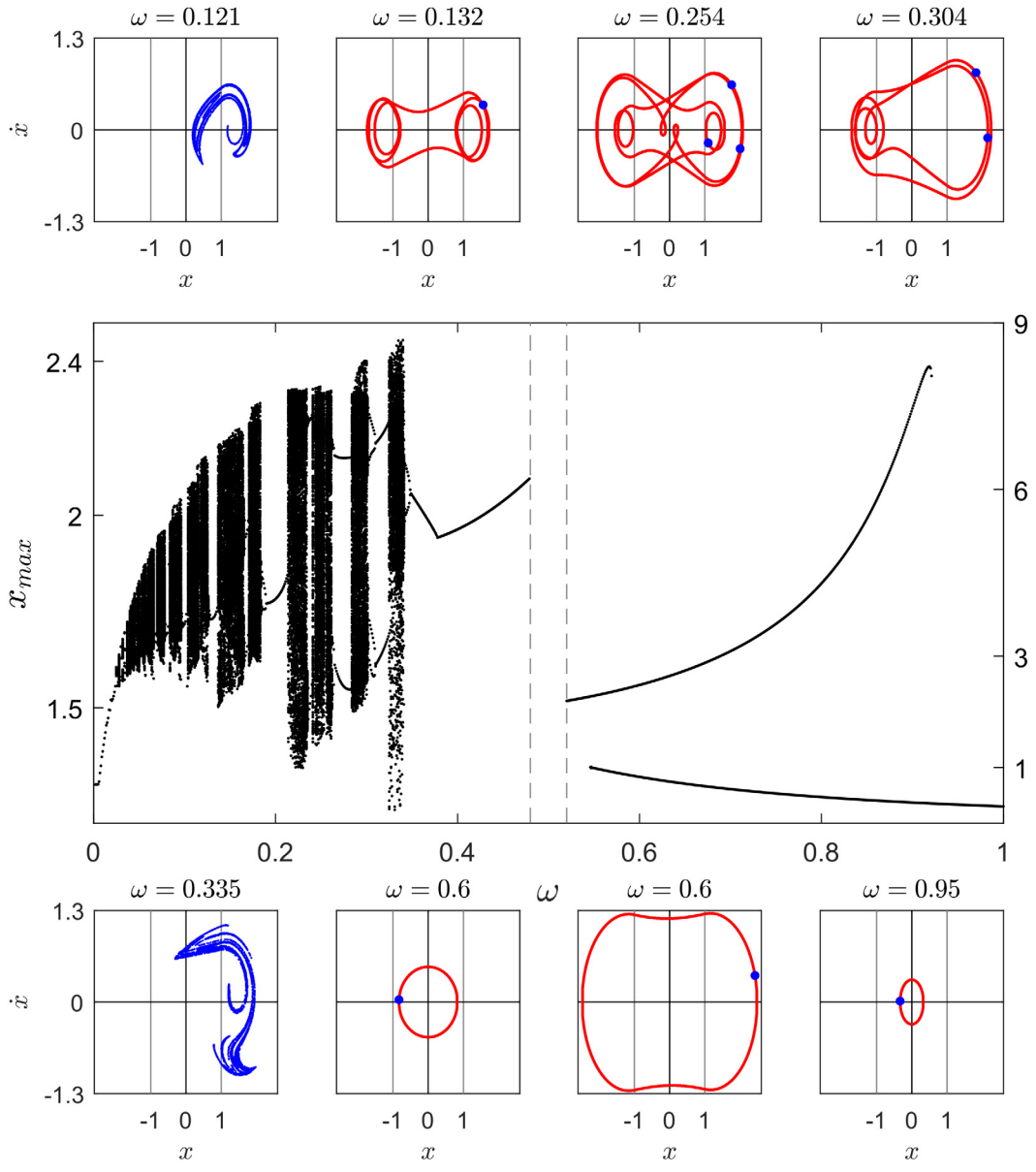

Fig. 2. Bifurcation diagram obtained by direct numerical simulation (central panel). Parameters are set as $a = 0.3$, $\beta = 0$, $\xi = 0.02$, $\alpha = 1$ and $e = 1$. Additional panels illustrate phase portraits for selected frequencies ω, where blue points represent stroboscopic Poincaré sections (sampling frequency set to ω) and red lines stand for trajectories. For $\omega = 0.121$ and $\omega = 0.335$: chaotic attractors; $\omega = 0.132$: multi-impact period-1 orbit; $\omega = 0.254$: symmetric period-3 orbit; $\omega = 0.304$: non-symmetric period-2 orbit; $\omega = 0.6$: coexistence of no-impact and single-impact period-1 orbits; $\omega = 0.95$: no-impacting period-1 orbit.

$(x, \dot{x})$ for different frequencies. For $\omega = 0.121$ and $\omega = 0.335$, chaotic attractors are observed. For $\omega = 0.304$ and $\omega = 0.254$, Poincaré sections indicate a periodicity greater than one with complex periodic motion. For $\omega = 0.6$, two coexisting attractors are present. One of them is a no-impact orbit while the other goes beyond the gap boundaries, both having period one. For $\omega = 0.132$ and $\omega = 0.95$, period-1 orbit with multi-impact and a non-impact are present respectively. These examples illustrate the variegated types of motion that can be observed in these systems.

3. Maps and stability analysis

Having regions of the system where the dynamics is described by linear equations is an advantage from the viewpoint of its analytical treatment. In this section, exact solutions within each of the regions are used to define mapping relationships and generate a systematic methodology to find global orbits. These maps are defined in Section 3.1. In

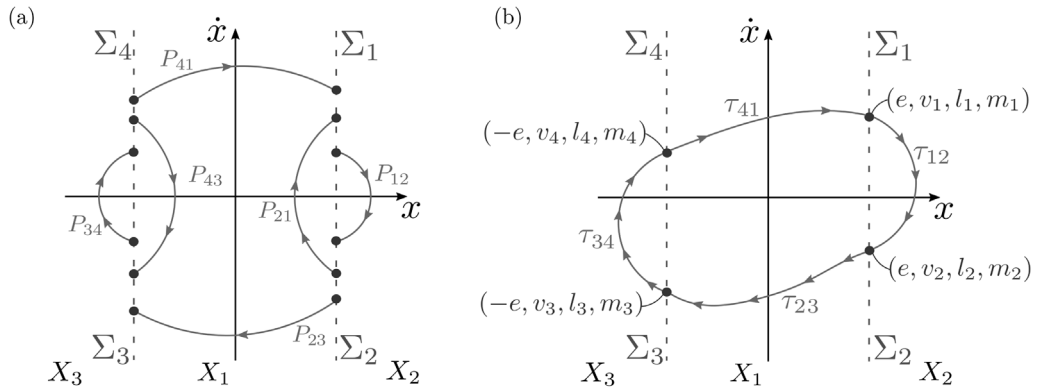

Fig. 3. (a) Three regions of the phase plane X_1, X_2 and X_3, the corresponding boundaries Σ_i, and the six mappings P_{ij}, are also depicted. (b) Schematic illustration of a non-symmetric period-1 solution. Values of τ_{ij} represent the time spent going from Σ_i to Σ_j.

Section 3.2, their application is illustrated through analysis of period-1 solutions, and in Section 3.3, a generalization of the method to more complex orbits is presented.

3.1. Trajectories and maps

The piecewise form of stiffness and damping functions, $k(x)$ and $c(x)$, naturally defines the regions $X_1 = \{(x, \dot{x}) : |x| \leq e\}$, $X_2 = \{(x, \dot{x}) : x > e\}$, and $X_3 = \{(x, \dot{x}) : x < -e\}$. The dynamics of the system in each region is governed by a linear ordinary differential equation. Switching between regions takes place at the discontinuity boundaries $\Sigma_1 = \{(x, \dot{x}) : x = e, \dot{x} > 0\}$, $\Sigma_2 = \{(x, \dot{x}) : x = e, \dot{x} < 0\}$, $\Sigma_3 = \{(x, \dot{x}) : x = -e, \dot{x} < 0\}$ and $\Sigma_4 = \{(x, \dot{x}) : x = -e, \dot{x} > 0\}$. Expressions for the displacement $x_i(\tau)$ and the velocity $\dot{x} = v_i(\tau)$ inside each subspace can be exactly obtained, and they are presented in Appendix A.

In order to describe any desired global trajectory of the dynamical system, six local maps can be defined:

$$\begin{aligned} &P_{12} : \Sigma_1 \to \Sigma_2; \quad P_{21} : \Sigma_2 \to \Sigma_1; \quad P_{23} : \Sigma_2 \to \Sigma_3; \\ &P_{34} : \Sigma_3 \to \Sigma_4; \quad P_{43} : \Sigma_4 \to \Sigma_3; \quad P_{41} : \Sigma_4 \to \Sigma_1. \end{aligned} \tag{5}$$

As illustrated in Fig. 3, each of these maps projects the point at which an orbit crosses one of the boundaries onto the following crossing of another boundary:

$$P_{ij} : (x_i, v_i, l_i, m_i) \to (x_j, v_j, l_j, m_j), \tag{6}$$

with $v_i = \dot{x}_i$. Here, we have introduced two new variables, $l_i = \cos(\omega\tau_i)$ and $m_i = \sin(\omega\tau_i)$, where τ_i is the time at which the orbit crosses Σ_i. According to the exact results presented in Appendix A, the maps have the form

$$P_{ij}\begin{pmatrix} x_i \\ v_i \\ l_i \\ m_i \end{pmatrix} = \begin{pmatrix} x_j \\ v_j \\ l_j \\ m_j \end{pmatrix} = A_k(\tau_{ij})\begin{pmatrix} x_i \\ v_i \\ l_i \\ m_i \end{pmatrix} + b_k(\tau_{ij}), \tag{7}$$

where A_k and b_k are matrices given by the parameters associated to the region X_k traversed going from Σ_i to Σ_j, and $\tau_{ij} = \tau_j - \tau_i$ is the time elapsed between the two crossings. The new variables l_i and m_i determine that the maps P_{ij} are linear, with a dependence on τ_{ij}. This addition has the advantage of making easier the construction of global solutions. On the other hand, it implies increasing the number of variables and requires imposing the additional condition $l_i^2 + m_i^2 = 1$. The analytical expressions for the matrices A_k and b_k are given in Appendix B.

3.2. Period-1 orbit

Once local maps are defined, global trajectories of the system can be constructed. To illustrate the method, let us consider the period-1 solution shown in Fig. 3(b). The sequence of local maps needed to assembly this solution is as follows:

$$P_{12} : (e, v_1, l_1, m_1) \to (e, v_2, l_2, m_2), \tag{8}$$

$$P_{23} \circ P_{12} : (e, v_1, l_1, m_1) \to (-e, v_3, l_3, m_3), \tag{9}$$

$$P_{34} \circ P_{23} \circ P_{12} = (e, v_1, l_1, m_1) \to (-e, v_4, l_4, m_4), \tag{10}$$

$$P_{41} \circ P_{34} \circ P_{23} \circ P_{12} : (e, v_1, l_1, m_1) \to (e, v_1, l_1, m_1), \tag{11}$$

The initial and final points of the complete sequence of maps, given by Eq. (11), are equal to (e, v_1, l_1, m_1), resulting in a closed period-1 orbit. Eqs. (8) to (10) represent the mapping sequences for some portion of the orbit. Using the matrix transformations of Appendix B and the additional condition $\tau_{12} + \tau_{23} + \tau_{34} + \tau_{41} = 2\pi\omega^{-1}$, which ensures that we obtain a period-1 orbit, these mapping sequences can be expressed as,

$$\begin{pmatrix} \pm e \\ v_j \\ l_j \\ m_j \end{pmatrix} = A(\tau_{12}, \tau_{23}, \tau_{34}) \begin{pmatrix} e \\ v_1 \\ l_1 \\ m_1 \end{pmatrix} + b(\tau_{12}, \tau_{23}, \tau_{34}), \tag{12}$$

where $A(\tau_{12}, \tau_{23}, \tau_{34})$ and $b(\tau_{12}, \tau_{23}, \tau_{34})$ represent the matrix product corresponding to each mapping sequence, and $(\pm e, v_j, l_j, m_j)$ is the final vector field of each of Eqs. (8)–(11). Note that these four equations are vector in nature, with four components each.

Finally, selecting the first component of Eqs. (8)–(10) and by an algebraic manipulation, the system variables v_1, l_1 and m_1 can be expressed in terms of times τ_{12}, τ_{23} and τ_{34}. By the combination of this result with the first two components of Eq. (11) and the additional condition $l_1^2 + m_1^2 = 1$, a set of three transcendental equations with three unknowns (τ_{12}, τ_{23} and τ_{34}) is obtained:

$$\mathcal{F}(\tau_{12}, \tau_{23}, \tau_{34}) = 0, \tag{13}$$

with $\mathcal{F} : \mathbb{R}^3 \to \mathbb{R}^3$. To solve this system of transcendental equations, we apply the multidimensional Newton's method. To catch all possible solutions for a given set of parameters, a multidimensional grid of time values is generated by dividing each time span into n intervals, using the fact that $0 < \tau_{ij} < 2\pi\omega^{-1}$. This grid is used to apply Newton's method taking each point as seed. After the whole set of simulations, a comparison of solutions and unification of the repeated instances is carried out.

After finding the solution of Eq. (13) for a given set of parameters, its stability must be assessed. Linear stability of a periodic solution is determined by the eigenvalues of the first derivative of the map, evaluated at the solution. The map governing the period-1 orbit of Fig. 3(b) can be written as

$$\mathbf{u}_{n+1} = \mathbf{P}(\mathbf{u}_n) = P_{41} \circ P_{34} \circ P_{23} \circ P_{12}, \tag{14}$$

where $\mathbf{u}_n = (v_n, l_n, m_n)$ represents the vector field of a given solution in the boundary Σ_1, and $\mathbf{u}_{n+1} = (v_{n+1}, l_{n+1}, m_{n+1})$ the corresponding vector field after one orbit –i.e. after one iteration of the map. Applying the chain rule, its first derivative is

$$D\mathbf{P} = \left(\frac{\partial \mathbf{u}_{i+4}}{\partial \mathbf{u}_i} \right)_{\mathbf{u}_n} = \left(\frac{\partial \mathbf{u}_{i+4}}{\partial \mathbf{u}_{i+3}} \right) \left(\frac{\partial \mathbf{u}_{i+3}}{\partial \mathbf{u}_{i+2}} \right) \left(\frac{\partial \mathbf{u}_{i+2}}{\partial \mathbf{u}_{i+1}} \right) \left(\frac{\partial \mathbf{u}_{i+1}}{\partial \mathbf{u}_i} \right) \Bigg|_{\mathbf{u}_n}, \tag{15}$$

where the subscripts represent each of the steps in the mapping sequence. Then, the partial derivatives of the Jacobian can be obtained by implicit derivation of the mappings. Therefore, the stability of the periodic orbit examined will be governed by the eigenvalues of the Jacobian matrix. If the module of the greatest eigenvalue is smaller than one the orbit will be stable. As shown in [29], the only possible bifurcations in these systems happen with the greatest eigenvalue λ of $D\mathbf{P}$ being real. Particularly, crossing of the stability limit $\lambda = -1$ gives period doubling bifurcation, while crossing $\lambda = +1$ gives a saddle–node or a pitchfork bifurcation.

3.3. Generalization to more complex orbits

A generalization of this method can be applied to find any other desired periodic orbit of this or similar piecewise linear systems. If N is the number of maps needed to describe the motion, the minimum of transcendental equations for the orbit will be equal to $N - 1$. To find these equations, we extend the procedure presented in the preceding section.

Let us consider a k-periodic orbit described by a sequence of N maps as follows:

$$\underbrace{P_{N\,1} \circ P_{N-1\,N} \circ \ldots \circ P_{23} \circ P_{12}}_{N \text{ maps}}. \tag{16}$$

Note that the sequence does not necessarily have to start with the map P_{12}, which is chosen here only to illustrate the process. The sequence of local maps that describe a portion of the trajectory are be given by

$$\begin{aligned} &\underbrace{P_{12}}_{\text{first local map}} \\ &\underbrace{P_{23} \circ P_{12}}_{\text{2 first local maps}} \\ &\vdots \\ &\underbrace{P_{n-1n} \circ \ldots \circ P_{12}}_{N-1 \text{ local maps}} \end{aligned} \tag{17}$$

Here a similar approach to that presented in the previous section should be performed. Taking the first two components of the global mapping sequence of Eq. (16), the first component of each of the local maps sequences of Eq. (17), the condition of $l_1^2 + m_1^2 = 1$ and the condition of k-periodic $\sum_{ij=12}^{N1} \tau_{ij} = 2k\pi\omega^{-1}$, a system of equation is obtained,

$$\mathcal{F}(\tau_{12}, \tau_{23}..., \tau_{N1}, v_1, l_1, m_1) = 0, \tag{18}$$

with $\mathcal{F} : \mathbb{R}^{N+3} \to \mathbb{R}^{N+3}$. This system has $N + 3$ equations with $N + 3$ unknowns, namely the unknowns the N elapsed times between boundaries (τ_{ij}) and the three components of the vector field of Point 1, (v_1, l_1, m_1).

However, to arrive at the least-order system that properly represents the solution, some additional algebraic manipulations must be done. To reduce the order of the system form $N + 3$ to N, the unknown variables (v_1, l_1, m_1) must be expressed in terms of the unknown times τ_{ij}. This is done by taking the first component of the first three local maps sequences of Eq. (17) and solving for the mentioned variables. The nature of the proposed semi-analytical method allows this with simple matrix manipulations. Finally, the k-periodic condition $\sum_{ij=12}^{N1} \tau_{ij} = 2k\pi\omega^{-1}$ naturally gives a dependency between one of the times τ_{ij} with the rest, and consequently reduces the order of the system by 1. In this way, the order of the system is now $N - 1$ and the least-order system that defines the solution is obtained,

$$\mathcal{F}'(\tau_{12}, \tau_{23}..., \tau_{N-1N}) = 0, \tag{19}$$

with $\mathcal{F}' : \mathbb{R}^{N-1} \to \mathbb{R}^{N-1}$. To solve this problem, a numerical method able to handle a system of transcendental equations must be applied. As pointed out in the preceding section, a strategy to explore multiple seeds must be applied, in order to find all possible solutions for each set of parameters.

The stability of the solutions can be studied applying the same methodology as for the period-1 orbit. The Jacobian matrix $D\mathbf{P}$ can be built using the chain rule:

$$D\mathbf{P} = \left(\frac{\partial \mathbf{u}_{i+N}}{\partial \mathbf{u}_i}\right)_{\mathbf{u}_n} = \underbrace{\left(\frac{\partial \mathbf{u}_{i+N}}{\partial \mathbf{u}_{i+(N-1)}}\right)\left(\frac{\partial \mathbf{u}_{i+(N-1)}}{\partial \mathbf{u}_{i+(N-2)}}\right)\ldots\left(\frac{\partial \mathbf{u}_{i+1}}{\partial \mathbf{u}_i}\right)\Bigg|_{\mathbf{u}_n}}_{N \text{ partial derivatives}}. \tag{20}$$

For eigenvalues lower than one the solution will be stable, and vice versa.

The procedure presented in this section can be used to find any desired periodic orbit of this system. The same method could be extended to build solutions of other piecewise systems, with the condition that exact solutions in each region are known.

4. Validation of the semi-analytical method

To validate the proposed semi-analytical method, a comparison with results of direct numerical integration is performed. Using the results presented in [43], several set of parameters are chosen with the aim of reproducing interesting behaviours and bifurcation phenomena. Before this, a sample case of the results obtained through the proposed semi-analytical method is presented. A characterization of the different types of solutions obtained is carried out.

Direct numerical simulations are performed by a Matlab routine that uses the 4th-order Runge–Kutta algorithm. We compute the complete time history starting from a given initial condition (x_0, v_0). Accuracy is essentially based on the size of the time step. Here, it is set to 5×10^{-4} times the force period T. To compute bifurcation diagrams, an initial transient equal to 100 periods is disregarded to allow for steady periodic orbits to develop, and 100 periods are recorded afterwards. For chaotic motion on Poincaré sections, 2000 extra periods were computed. A tolerance parameter of 5×10^{-5} is set to evaluate the convergence of phase portrait values after one period. A typical bifurcation diagram and phase portraits for the selected frequencies are presented in Fig. 2.

To implement the proposed semi-analytical method, a code is developed using Matlab function `fsolve`, which solves implicit systems of nonlinear equations of the form $F(X) = 0$. The optimization parameters of this function are set to `TolFun` $= 10^{-10}$ and `TolX` $= 10^{-10}$ to have a proper convergence in the algorithm. To evaluate all possible solutions for a given set of parameters of Eq. (13), multiple seeds (τ_{12}, τ_{23}, τ_{34}) must be considered. To do this, each interval $0 < \tau_{ij} < T$ is divided into 8 points, thus having a grid of $8^3 = 512$ different seed values for each parameter set. After running all these simulations and properly evaluating the stability and symmetry of the obtained solutions, bifurcation and phase diagrams are constructed to illustrate the results.

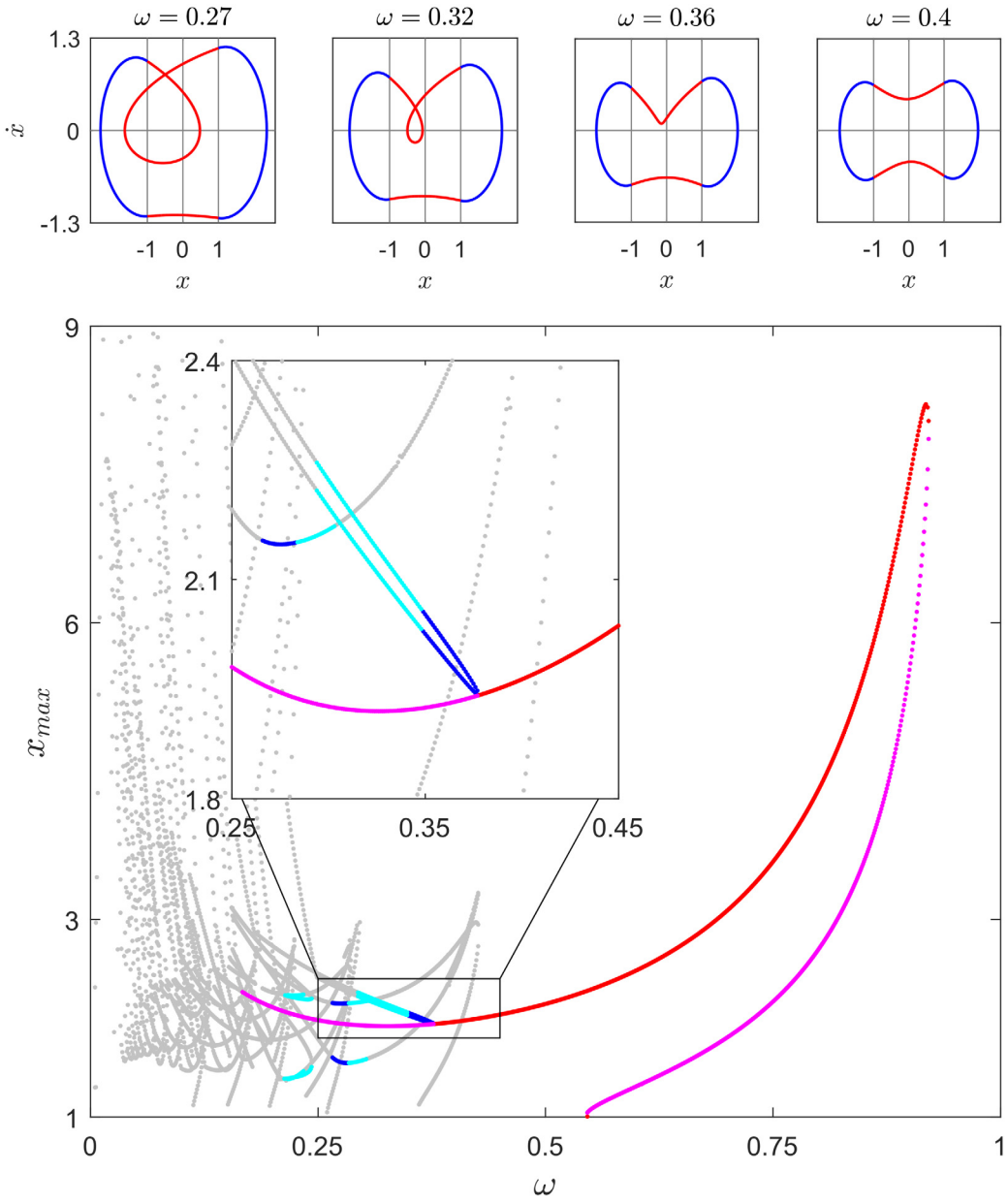

Fig. 4. Bifurcation diagram obtained with our new semi-analytical method. Parameters are set as $a = 0.3$, $\beta = 0$, $\xi = 0.02$, $\alpha = 0$ and $e = 1$. Red and pink are used to mark symmetric stable and unstable orbits, blue and cyan are used for non-symmetric stable and unstable ones, and grey points represent non-physical solutions. Additional panels illustrate phase portraits for selected frequencies ω where blue and red colour are used to illustrate the trajectory inside ($|x| < e$) and outside ($|x| > e$) the gap respectively.

4.1. Physical and non-physical bifurcation scenarios obtained by the semi-analytical method

Fig. 4 presents a typical bifurcation diagram obtained by our method. The additional panels illustrate diverse archetypic trajectories. For $\omega = 0.4$, a stable symmetric orbit is obtained. As the frequency decreases, this orbit remains stable until $\omega = 0.378$, where a pitchfork bifurcation takes place, making the symmetric motion unstable and generating two non-symmetric stable orbits. For $\omega = 0.36$ and $\omega = 0.32$ non-symmetric stable and unstable orbits are obtained, respectively. The change in stability takes place at $\omega = 0.349$, where the largest eigenvalue of the Jacobian crosses $\lambda = -1$. Finally, for $\omega = 0.27$ a non-physical orbit is obtained.

Non-physical orbits are defined as those where the number of crossings of the boundaries Σ_i is larger than the number postulated in the map sequence. The mapping technique links points located on the boundaries between regions, but

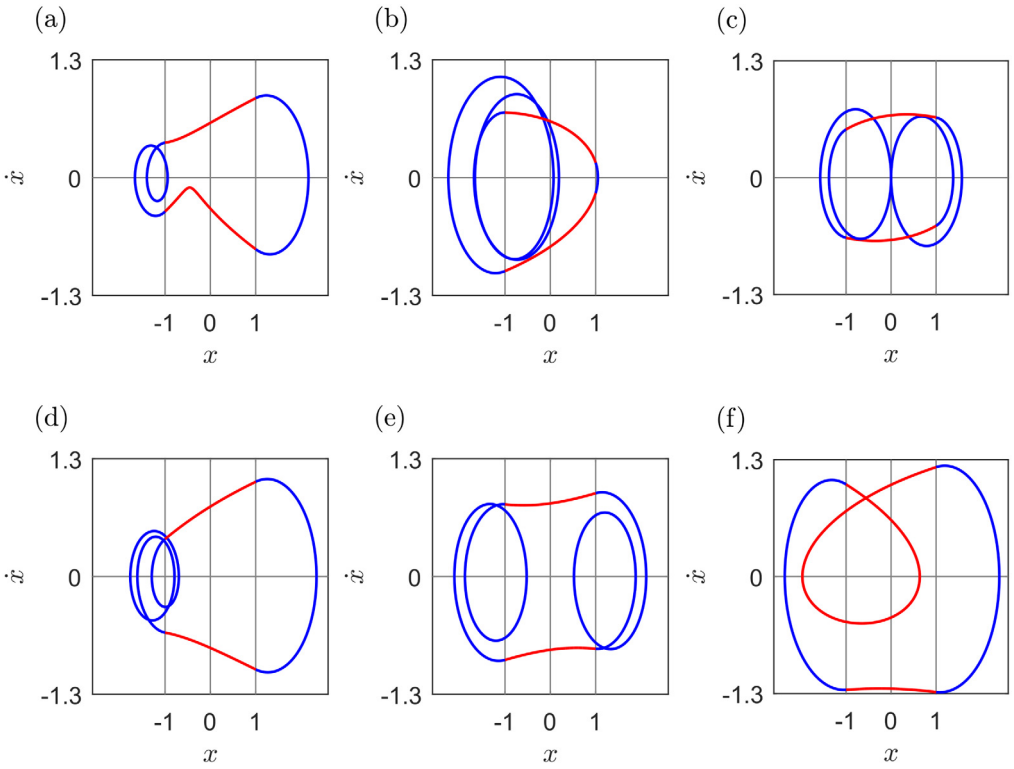

Fig. 5. Six different non-physical orbits obtained with the proposed method for excitation frequency of $\omega = 0.26$ and the same parameters as in Fig. 4. Red colour is used to mark the trajectory described by the solution inside the gap ($|x| < e$) and blue colour for the trajectory described by the solution outside the gap ($|x| > e$).

does not limit the domain that the trajectory covers to join both points. For this reason, it is possible to obtain orbits that occasionally cover more than one region with a single map. These solutions do not make physical sense, since moving through the regions changes the parameters of the equation of motion, and consequently, a new sequence of maps must be postulated to properly reproduce the obtained solution. In the particular case for $\omega = 0.27$ shown in Fig. 4, a loop is observed in the top-left of the phase portrait. This implies two extra boundary crossings (one at Σ_3 and another one at Σ_4) for the unique map P_{41} to join boundary Σ_4 with Σ_1. Consequently, a such solution is characterized as non-physical because the correct sequence to describe that portion of the trajectory is $P_{41} \circ P_{34} \circ P_{43}$.

To determine if a solution is non-physical, we verify that the trajectory remains within a single region for each local map. This is done by applying the following conditions to each of the solutions: $x > e, \forall(x, \dot{x}) \in P_{12}$, $x < -e, \forall(x, \dot{x}) \in P_{34}$ and $|x| < e, \forall(x, \dot{x}) \in P_{ij}$ with $ij \neq 12, 34$. These conditions must be checked for all the obtained solutions of Eq. (18). For instance, for the local map P_{41}, the trajectory must remain in X_1 region, which mathematically is described as $|x| < e, \forall(x, \dot{x}) \in P_{41}$. This condition is not fulfilled for the solution of $\omega = 0.27$ of Fig. 4, and therefore it is classified as non-physical.

Different types of non-physical solutions are presented in Fig. 5 for $\omega = 0.26$. Panel 5(a) depicts a situation where a small loop on the left side of phase portrait has an extra cross of the boundaries Σ_3 and Σ_4. For this case some similar solution, properly defined by the proposed method, might be found by postulating the sequence $P_{41} \circ P_{34} \circ P_{43} \circ P_{34} \circ P_{23} \circ P_{12}$. Panels 5(c) and (e) show symmetric cases of non-physical solutions, where additional crossing of the four boundaries Σ_i occur. Case 5(f) is a situation similar that shown in Fig. 4, where a small loop in the central zone starts to grow until its size generates an additional crossing of the limit $x = -1$. Fig. 5(b) and (d) represent non-symmetrical solutions with an important difference between the size of the orbit at both sides of the phase diagram.

These non-physical solutions will be discarded henceforth in this work. As can be seen in Fig. 4, the typical structure of the bifurcation diagram remains present in the region of these solutions. Future investigations can be carried out to determine if these structures can be used to describe the behaviour of the system beyond the region of period-1 solutions.

4.2. Validation of the method

To validate the proposed semi-analytical method in Fig. 6 the bifurcation diagrams obtained with both methods are presented together. As observed the proposed method makes an exact prediction of the different bifurcation scenarios.

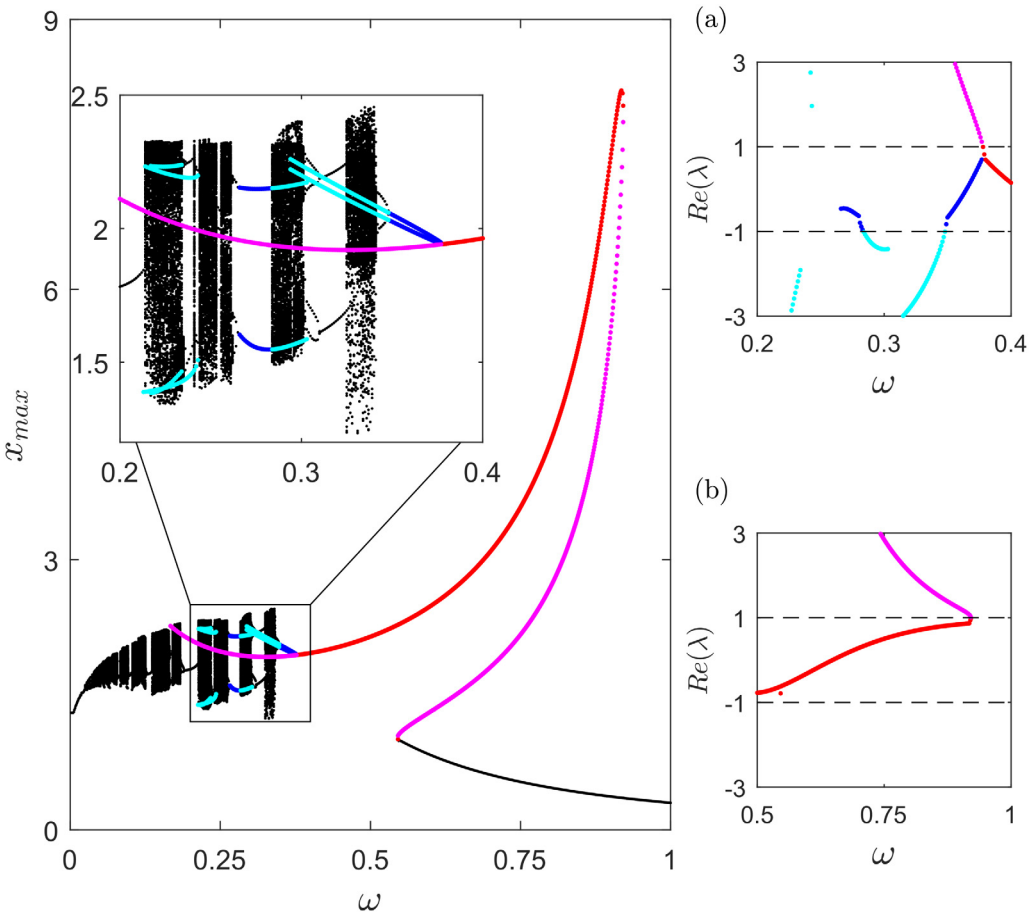

Fig. 6. Superposition of bifurcation diagrams from Figs. 2 and 4. Red and pink are used to mark symmetric stable and unstable orbits, blue and cyan are used for non-symmetric stable and unstable ones, and black points mark the results for numerical integration method. A precise correlation is observed between the results of both methods. Zoom area correspond to $0.2 < \omega < 0.4$, and show a precise prediction of period-doubling phenomena. The additional panels on the right illustrate the evolution of the real part of the eigenvalues of the Jacobian for the solutions obtained with the proposed method (frequency regions are (a) $0.2 < \omega < 0.4$ and (b) $0.8 < \omega < 1$).

Also a very good correlation between obtained phase portraits is observed. Stable period-1 orbits determined by the proposed method has an exact correlation with those obtained by direct numerical integration results. The difference between the values of x_{max} obtained with both methods is presented in Fig. 7(a) and (b) for two different ranges of ω. The maximum difference is less than 0.01% between the methods, which represents a good correlation. The unstable orbits presented in Fig. 4 are not possible to reproduced with direct integration method and in Fig. 6 it can be seen how unstable period-1 orbits co-exist with other types of motion like period-2, period-3 or chaotic.

The right-hand panels of Fig. 6 show the dependence of the real part of the eigenvalues of the Jacobian matrix on the frequency. Sudden changes in the slope of the eigenvalues evolution close to bifurcations is obtained in all cases. These changes correspond to the frequencies where the imaginary part of the eigenvalues become zero, as presented in Fig. 8. Fig. 6(a) presents the range $0.2 < \omega < 0.4$. Two period-doubling scenarios are obtained for $\omega = 0.283$ and $\omega = 0.349$, and a pitchfork bifurcation occurs at $\omega = 0.378$. Fig. 6(b) depicts the range $0.8 < \omega < 1$, where two saddle–node bifurcations take place at $\omega = 0.546$ (close to the grazing condition) and $\omega = 0.921$.

In Fig. 9, bifurcation diagrams of displacement as a function of the damping ratio (ξ), obtained with our method and by direct numerical integration, are shown. Again, a very good agreement between predictions of both methods is obtained. For $\xi = 0.0153$, the non-symmetric period-1 solution becomes unstable, which corresponds to the appearance of period-doubling phenomena. Between $0.0153 < \xi < 0.1033$, three coexisting unstable period-1 orbits are predicted, one of them symmetric and two non-symmetric. In the same region, chaotic and periodic orbits with periodicity greater than one are computed by direct numerical integration. For $\xi = 0.04$ and $\xi = 0.075$, additional panels in Fig. 9 present chaotic attractors, for $\xi = 0.02$ we find a period-2 orbit and for $\xi = 0.0583$ one of period-3. For $0.1033 < \xi < 0.1773$ period-1 non-symmetric orbits become again stable (see the case $\xi = 0.11$ in Fig. 9), but for $0.1235 < \xi < 0.1736$ these period-1 solutions become non-physical because the orbit for this range has a small loop with an extra crossing to boundaries Σ_1

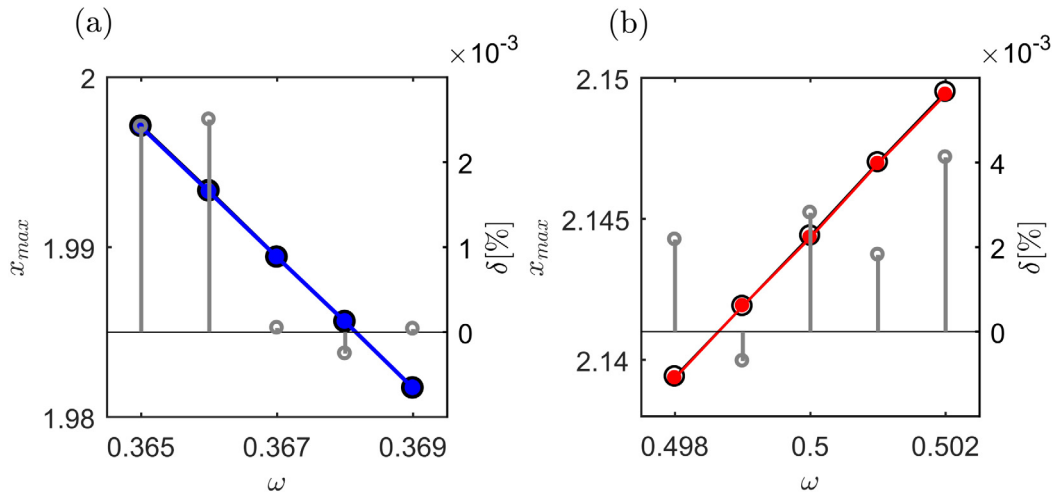

Fig. 7. Difference of x_{max} values (grey colour) obtained with both methods for two selected regions in Fig. 6; (a) for $0.365 \leq \omega \leq 0.369$ largest value of δ is less than 0.0025%; (b) for $0.498 \leq \omega \leq 0.502$ the largest value of δ is around 0.0042%. Blue and red are used to mark symmetric and non-symmetric semi-analytical solutions, respectively. The black circles mark the solutions obtained by direct numerical integration.

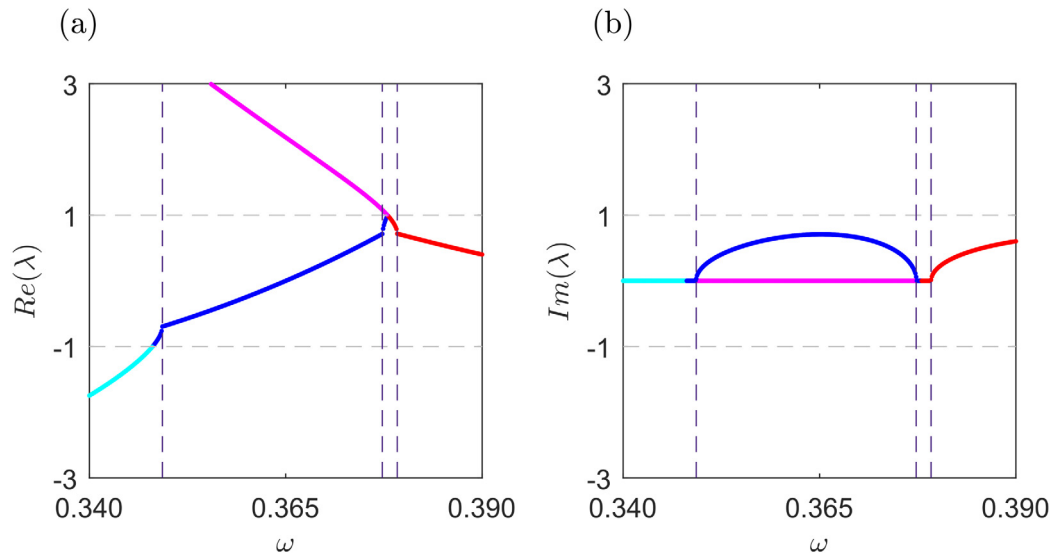

Fig. 8. Evolution of real (a) and imaginary (b) part of the eigenvalues in therms of excitation frequency. A smaller range of values ($0.34 < \omega < 0.39$) for system parameters correspond to Fig. 4 is presented. Vertical dashed lines indicates the frequencies where the imaginary part become zero, having an exact correspondence with the change in the slope of the real part ($\omega = 0.3493$, $\omega = 0.3773$ and $\omega = 0.3792$).

and Σ_2 (see case $\xi = 0.15$ in Fig. 9). Finally, for $\xi = 0.1773$ a pitchfork bifurcation occurs, giving a period-1 symmetric orbit as the stable condition for $0.1773 < \xi < 0.2$.

5. Effect of stiffness

Once the validation of the semi-analytical method has been carried out, it can be used to study the behaviour of the system under certain variations of parameters. In this section the influence of stiffness function definition is investigated. For this purpose, two alternative situations are analysed. In case A the stiffness function is modified in such a way that the value of k_2, which defines the stiffness inside the gap ($|x| < e$), is kept constant, while outside the gap ($|x| > e$) k_1 is varied. In case B the opposite situation is considered. In both cases, all the other original parameters are held constant, but their non-dimensional counterparts vary according to the changes in k_1 or k_2 (see Tables 1 and 2). As it has been done in a preceding section, period-1 solutions are investigated by application of the semi-analytical method to the mapping sequence of Eq. (11).

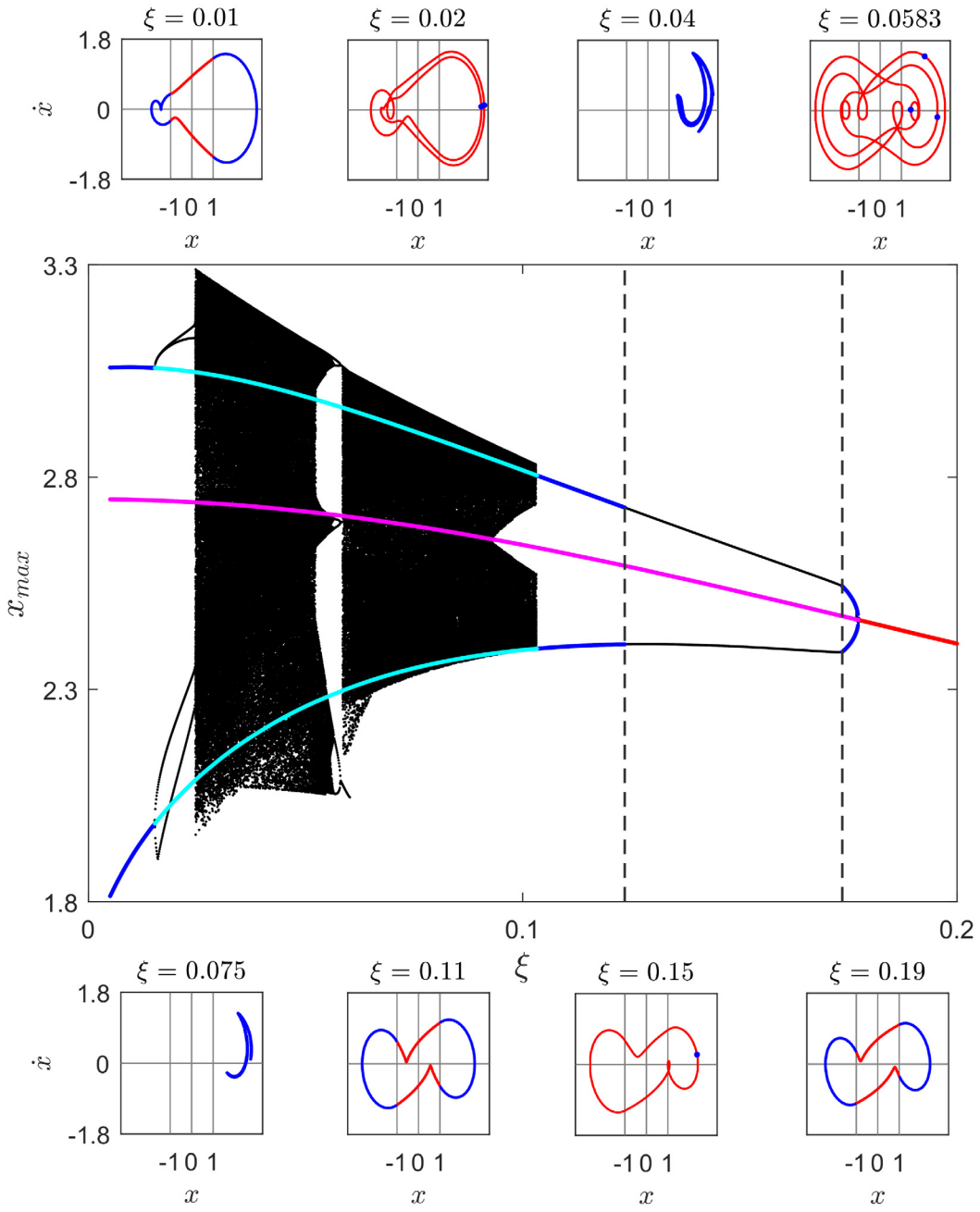

Fig. 9. Superposition of bifurcation diagrams obtained by direct numerical integration and proposed semi-analytical method. System parameters are set as $a = 0.7$, $\beta = 0$, $\omega = 0.3$, $\alpha = 0$ and $e = 1$. Red and pink are used to mark symmetric stable and unstable orbits, blue and cyan are used for non-symmetric stable and unstable ones, and black points mark the results for numerical integration method. Additional panels illustrate phase portrait for the analytical method at damping values of $\xi = 0.01$, $\xi = 0.11$ and $\xi = 0.19$. Phase portrait and Poincaré section for $\xi = 0.02$, $\xi = 0.0583$ and $\xi = 0.15$ and chaotic attractor for $\xi = 0.04$ and $\xi = 0.075$, correspond to results obtained with the numerical integration method. Note that for range $0.1235 < \xi < 0.1736$ marked by dashed lines, the two black lines represent the two non-symmetric period-1 solutions obtained by direct numerical integration with different initial conditions and not a period-2 solution.

Fig. 10(a) presents the six bifurcation diagrams for the different cases listed in Table 1. To facilitate a visual comparison between the diagrams, the forcing frequency Ω is used as the bifurcation parameter, instead of the dimensionless frequency ω used for previous figures. This correspond with the fact that the two grazing frequencies for cases A1 to

Table 1
Non-dimensional parameters for case A. Original parameters are $m = 1$, $G = 1$, $A = 0.8$, $c_1 = 0$, $c_2 = 0.2$ and $y_0 = 1$. Stiffness inside the gap is held constant at $k_2 = 2$.

Case	β	a	ξ	ω_n	α	e
A1 ($k_1 = -1.5$)	4	1.6	0.1414	0.7071	1	1
A2 ($k_1 = -1$)	2	0.8	0.1	1	1	1
A3 ($k_1 = -0.5$)	1.33	0.53	0.0816	1.2247	1	1
A4 ($k_1 = 0.5$)	0.8	0.32	0.0632	1.5811	1	1
A5 ($k_1 = 1$)	0.66	0.27	0.0577	1.7321	1	1
A6 ($k_1 = 2$)	0.5	0.2	0.05	2	1	1

Table 2
Values of non-dimensional parameters for case B. Original parameters are $m = 1$, $G = 1$, $A = 0.3$, $c_1 = 0$, $c_2 = 0.16$ and $y_0 = 1$. Stiffness outside the gap is held constant at $k_1 = 1$.

Case	β	a	ξ	ω_n	α	e
B1 ($k_2 = 1$)	0.5	0.15	0.0566	1.4142	1	1
B2 ($k_2 = 0.75$)	0.43	0.17	0.0605	1.3229	1	1
B3 ($k_2 = 0.5$)	0.33	0.2	0.0653	1.2247	1	1
B4 ($k_2 = 0.25$)	0.2	0.24	0.0716	1.118	1	1
B5 ($k_2 = 0.05$)	0.0476	0.2857	0.0781	1.0247	1	1
B6 ($k_2 = 0$)	0	0.3	0.08	1	1	1

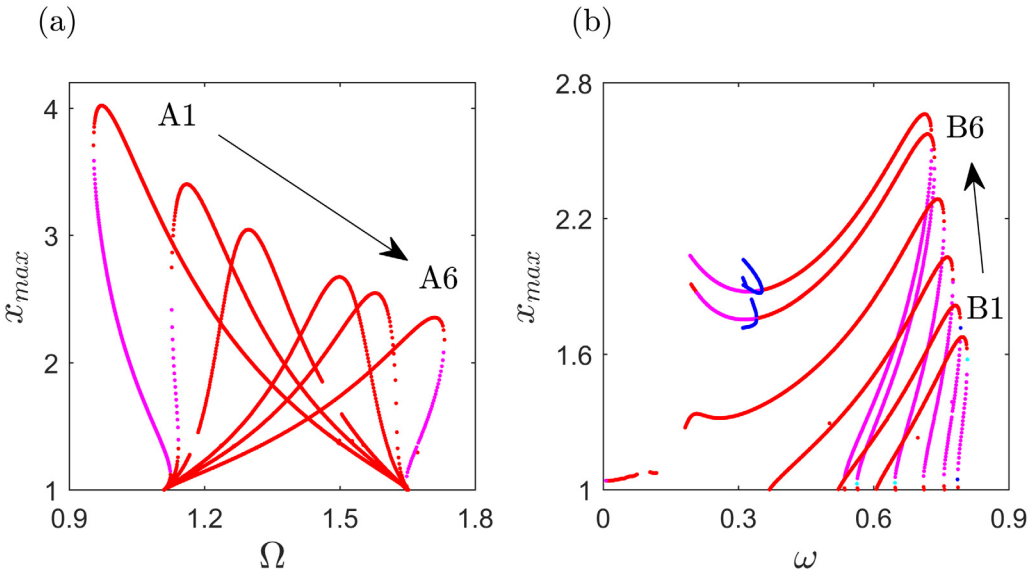

Fig. 10. Different bifurcation diagrams for: (a) cases A1 to A6 as listed in Table 1 where dimensional excitation frequency Ω is used as the bifurcation parameter; (b) cases B1 to B6 as listed in Table 2, where dimensionless excitation frequency ω is used as the bifurcation parameter. Red and pink are used to mark symmetric stable and unstable orbits, blue and cyan are used for non-symmetric stable and unstable ones.

A6 are the same, calculated by setting the amplitude of the linear solution inside the gap ($|x| < e$) equal to one. This occurs because the stiffness inside the gap is the same for all the cases.

As observed in this figure, a typical softening behaviour for cases A1, A2 and A3 is obtained. Note that for these cases stiffness ratio β is greater than one, which means that the stiffness inside the gap is bigger than outside. The value of β is also related to the maximum amplitude reached, as β grows there is an increase in the maximum amplitude of the peak of the diagram. For cases A4, A5 and A6, hardening bifurcations diagrams are obtained. This correspond to the fact that $\beta < 1$ and stiffness outside the gap is bigger than inside. Moderate differences between the slope of the stiffness function inside and outside the gap generate bifurcation diagrams slightly shifted to the left (soft) or right (hard), but without the presence of unstable orbits and therefore saddle–node bifurcations. This is the situation for cases A3, A4 and A5, whose β parameter are close to one, corresponding to a small difference in stiffness slope at both sides of boundaries. On the opposite side, cases A1, A2 and A6 have β values with a larger difference with the linear case $\beta = 1$, and in consequence the bifurcations diagrams present richer non-linear behaviours like multiple solutions for some system parameters, saddle–node bifurcations and unstable orbits.

Fig. 10(b) the bifurcation diagrams for the six different system parameters indicated in Table 2 are presented. Dimensionless forcing frequency ω is used here as the bifurcation parameter. All the cases present a hardening behaviour,

Table 3
Values of non-dimensional parameters for case C. Constant values of original parameters are $m = 1$, $G = 1$, $A = 0.6$, $k_1 = 0$, $k_2 = 1$ and $y_0 = 1$. Viscous damping inside the gap is held constant at $c_2 = 0.4$, and c_1 values are indicated for each case in the table.

Case	β	a	ξ	ω_n	α	e
C1 ($c_1 = -0.36$)	1	0.6	0.02	1	10	1
C2 ($c_1 = -0.3$)	1	0.6	0.05	1	4	1
C3 ($c_1 = 0$)	1	0.6	0.2	1	1	1
C4 ($C_1 = 0.4$)	1	0.6	0.4	1	0.5	1
C5 ($C_1 = 0.8$)	1	0.6	0.6	1	0.33	1

Table 4
Values of non-dimensional parameters for case D. Constant values of original parameters are $m = 1$, $G = 1$, $A = 0.3$, $k_1 = 1$, $k_2 = 0$ and $y_0 = 1$. Viscous damping outside the gap is held constant at $c_1 + c_2 = 0.16$, but values of c_1 and c_2 vary for each case as indicated in the first column of the table.

Case	β	a	ξ	ω_n	α	e
D1 ($c_1 = -0.64$, $c_2 = 0.8$)	0	0.3	0.08	1	5	1
D2 ($c_1 = -0.08$, $c_2 = 0.24$)	0	0.3	0.08	1	1.5	1
D3 ($c_1 = 0.08$, $c_2 = 0.08$)	0	0.3	0.08	1	0.5	1
D4 ($c_1 = 0.14$, $c_2 = 0.02$)	0	0.3	0.08	1	0.125	1

characterized by the bending of the peak of the diagram to the high frequency region. This corresponds to the fact that, for case B, all parameters give values of stiffness ratio $\beta < 1$. Cases B4, B5 and B6 present a single cutoff of the limit $x_{max} = 1$, meaning a single frequency with grazing condition for the linear solution inside the gap. This situation is related to the occurrence of more complex behaviour and bifurcation scenarios. In particular, pitchfork bifurcations take place in cases B5 and B6 for $\omega = 0.341$ and $\omega = 0.353$, respectively. As seen in the preceding sections, pitchfork bifurcations in these systems imply the apparition of non-symmetric period-1 solutions, that then could be followed by period-doubling bifurcations and associated more complex orbits. On the other hand, cases B1 to B3 present two frequencies where $x_{max} = 1$, and consequently only saddle–node bifurcation scenarios and symmetric orbits.

The main result of the analysis of case B is related to the condition of a single crossing of the limit $x_{max} = 1$, associated with the appearance of more complex behaviours and pitchfork bifurcations. This condition can be analytically described by setting the amplitude of the linear solution inside the gap equal to one, which is equivalent to

$$(\beta - \omega^2)^2 + (2\alpha\xi\omega)^2 - a^2 = 0. \tag{21}$$

To have real solutions of Eq. (21),

$$\alpha\xi^4 - 2\alpha\xi^2\beta + a^2 > 0 \tag{22}$$

must hold, and to have only a single solution, it is necessary that

$$\beta^2 < a^2. \tag{23}$$

Therefore, Eqs. (22) and (23) are necessary but not sufficient conditions for having more complex dynamical responses, like multi-period solutions of even chaotic orbits.

6. Effect of damping

As another example of how our method could be applied to investigate the dynamics of piecewise linear systems, in this section the effects associated with variations in the viscous damping function is studied in two different cases. In case C, the damping function is modified in such a way that the value of the viscosity c_2 inside the gap ($|x| < e$) is kept constant, while the viscosity c_1 is varied to have different viscous damping outside the gap ($|x| > e$). In case D, diverse situations with the same viscous damping outside the gap ($|x| < e$) are analysed by keeping constant $c_1 + c_2$, but with different values of damping inside the gap. As in the preceding section, all other original parameters are held constant, but their non-dimensional counterparts vary according to changes in c_1 or c_2 (see Tables 3 and 4). To analyse differences between both cases, period-1 solutions are investigated by the application of the our method to the mapping sequence of Eq. (11).

Fig. 11(a) depicts a plot of all the bifurcation scenarios for the parameters indicated in Table 3. For this case the dimensionless frequency ω is used as the bifurcation parameter, noting that $\Omega = \omega$, due to the fact that for all the cases in Table 3 $\omega_n = 1$. The five diagrams in Fig. 11(a) present the same crossover frequency of the conditions $x_{max} = 1$. The value of these cutoff frequencies is related to the definition of the system parameters within the gap. Note that all cases in Table 3 have the same parameter settings for $|x| < e$.

The results reveal a difference between the behaviour of the system depending on whether $\alpha > 1$ or $\alpha < 1$, exhibiting some similarity with the hardening and softening situations associated with the value of β in case A. In cases C1 and

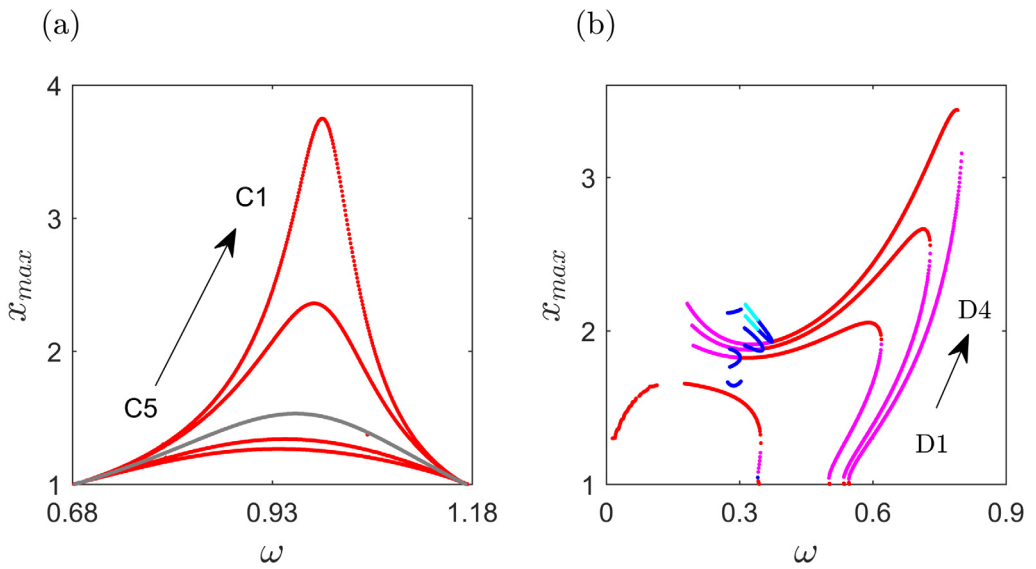

Fig. 11. Bifurcation diagrams with ω used as the bifurcation parameter and computed for (a) cases C1 to C5 as listed in Table 3, where red dots indicates symmetric stable orbits, grey colour is also used to plot symmetric stable orbits but only for case C3, indicating that this represent the pure linear situation ($\alpha = 1$ and $\beta = 1$); (b) cases D1 to D4 as listed in Table 4, where red dots indicates symmetric stable orbits, pink symmetric unstable, blue and cyan mark stable and unstable non-symmetric orbits respectively.

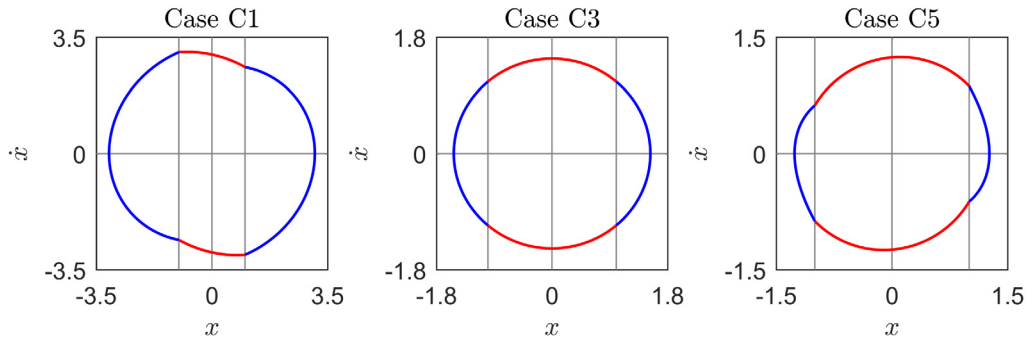

Fig. 12. Phase portraits for $\omega = 0.96$ for cases C1, C3 and C5 in Table 3. A non-smooth change in slope of the orbit in the boundaries Σ_i, is observed for each of the cases.

C2, the viscous damping inside the gap is bigger than outside, so that $\alpha > 1$. Diagrams show the biggest values of the maximum amplitude, and a displacement to higher frequencies of these peaks. For cases C4 and C5 the opposite behaviour is obtained: the peak in the bifurcation diagram moves to smaller frequencies and its associate maximum amplitude decreases. Making a comparison with the results of case A, in case C the peaks that move to higher frequencies present an increment of the maximum amplitude, instead of the decrements observed in Fig. 10(a). But a more interesting result of this comparison is the fact that for case C the non-linearity introduced by the discontinuity of the damping function does not generate the apparition of saddle–node bifurcations and the associated unstable orbits.

The three panels in Fig. 12 show the effect of a non-smooth change in damping force, that generates a change in the slope of the phase portrait when crossing any of the boundaries Σ_i. Note that the slope of the phase portrait is directly related to the evolution of the system acceleration $\ddot{x}$. Form Eq. (1) the acceleration can be expressed as,

$$\ddot{x} = a\cos(\omega\tau) - c(x)\dot{x} - k(x). \tag{24}$$

Eq. (24) demonstrate how non-smooth changes in damping force (associated with $c(x)$ function) generate different values of $\ddot{x}$ at both sides of the boundaries Σ_i. Therefore, configurations with $\alpha \neq 1$ will present a non-smooth phase portrait related to this change on slope. How far is α from 1 will determine the degree of non-smoothness, and the sign of the change of slope will be given by whether α is greater or smaller than one, in agreement with the results presented in Fig. 12.

In Fig. 11(b) bifurcation diagrams for the four different parameter sets indicated in Table 4 is presented. The dimensionless forcing frequency ω is used here as the bifurcation parameter. For all cases, results reveal a hardening

behaviour, related to the setting of the parameter $\beta = 0$. In this situation, the effect of variations in the damping function is associated with the possibility, or not, of having pitchfork bifurcations and related non-symmetric orbits. For cases D2, D3 and D4 this type of bifurcation takes place, but for case D1 it never appears, and symmetric orbits remain stable even for small frequencies. This behaviour is related to the value of the product $\alpha\xi$, representing the damping ratio inside the gap. As this product increases, the damping ratio for $|x| < e$ also increases and therefore the appearance of pitchfork bifurcations and non-symmetric orbits is inhibited. This fact shows how an increase in viscous damping can act as an impediment to the appearance of non-symmetrical orbits, the subsequent period doubling bifurcations, and the possibility of having chaotic orbits.

7. Conclusions

A semi-analytical method capable to describe and analyse any periodic orbit of a piecewise linear oscillator with a harmonic excitation was presented. All the local maps of the system were developed using the available analytical solution in each region of the domain. Based on the local maps, and by the expansion of vector field with two new variables $l = \cos(\omega\tau)$ and $m = \sin(\omega\tau)$, we arrived with the minimum order transcendental system of equation was developed. The proposed change of variables allows for a simple implementation of the sequence of mappings and, therefore, implies an important advantage in the algebraic handling of the equations. For a given orbit, described by a number N of mappings, it was shown that a minimum order $N - 1$ is obtained for the transcendental system of equations that describes this solution.

To validate the proposed semi-analytical method comparisons against brute-force numerical results was performed. Particularly, the mapping sequence for period-1 solutions was investigated for parameter sets obtained from [43]. A very good agreement between the two methods was observed, and the proposed methodology was capable to capture all relevant bifurcation situations. A significant number of obtained solutions were classified as non-physical, because they presented some inconsistencies between the postulated maps sequence and the trajectory described by the solution. This set of solutions has been discarded for the scope of this work, but a deeper understanding of their behaviour and structures could be a useful to gain a greater insight into piecewise linear systems.

Two practical cases of how the semi-analytical method can by applied to the study of piecewise linear system were presented in Sections 5 and 6. In the first of them, the influence of different stiffness function definition was investigated. It was found that a pitchfork bifurcation, which makes the symmetric orbits unstable and the asymmetric ones stable, is the starting point for a period-doubling cascade, and the subsequent appearance of chaotic motion. Associated with this, a series of minimum conditions that must be met by the system for this phenomenon to occur was defined. In Section 6, the influence of viscous damping was investigated. Our results show how an increase in damping can control the appearance of non-symmetrical orbits, doubling phenomena and more complex behaviour.

CRediT authorship contribution statement

Agustín Hernández Rocha: Investigation, Validation, Writing – original draft. **Damián H. Zanette:** Methodology, Reviewing, Supervision. **Marian Wiercigroch:** Conceptualization, Methodology, Writing, Reviewing, Supervision.

Declaration of competing interest

The authors declare that they have no known competing financial interests or personal relationships that could have appeared to influence the work reported in this paper.

Data availability

No data was used for the research described in the article.

Acknowledgements

The authors would like to thank the Balseiro Institute and the National Commission of Atomic Energy for the support. In particular, financial support for the Invited Professor Programme of the Balseiro Institute, which made international collaboration possible.

Appendix A. Linear solutions of Eq. (1) in each region

Expressions for position and velocity in region X_1, for given initial conditions $x_1(\tau_n) = x_n$ and $v_1(\tau_n) = v_n$, are:

$$x_1(\tau) = C_1 \exp^{\lambda_1(\tau-\tau_n)} + C_2 \exp^{\lambda_2(\tau-\tau_n)} + C_3 \cos(\omega\tau + \phi_1), \tag{A.1}$$

$$v_1(\tau) = \lambda_1 C_1 \exp^{\lambda_1(\tau-\tau_n)} + \lambda_2 C_2 \exp^{\lambda_2(\tau-\tau_n)} - \omega C_3 \sin(\omega\tau + \phi_1), \tag{A.2}$$

where constants are:

$$\lambda_{1,2} = -\alpha\xi \pm \sqrt{(\alpha\xi)^2 - \beta^2}, \tag{A.3}$$

$$\tan(\phi_1) = -\frac{2\alpha\xi\omega}{\beta - \omega^2}, \tag{A.4}$$

$$C_3 = \frac{a}{\sqrt{(\beta-\omega^2)^2 + (2\alpha\xi\omega)^2}}, \tag{A.5}$$

$$C_1 = \frac{\lambda_2 x_n - v_n - C_3[\lambda_2 \cos(\omega\tau_n + \phi_1) + \omega \sin(\omega\tau_n + \phi_1)]}{\lambda_2 - \lambda_1}, \tag{A.6}$$

$$C_2 = \frac{\lambda_1 x_n - v_n - C_3[\lambda_1 \cos(\omega\tau_n + \phi_1) + \omega \sin(\omega\tau_n + \phi_1)]}{\lambda_1 - \lambda_2}. \tag{A.7}$$

Expressions for position and velocity in regions X_2 and X_3, for given initial conditions $x_{2,3}(\tau_n) = x_n$ and $v_{2,3}(\tau_n) = v_n$, are:

$$x_{2,3}(\tau) = \pm(1-\beta)e + C_{4,7} \exp^{\lambda_3(\tau-\tau_n)} + C_{5,8} \exp^{\lambda_4(\tau-\tau_n)} + C_6 \cos(\omega\tau + \phi_2), \tag{A.8}$$

$$v_{2,3}(\tau) = \lambda_3 C_{4,7} \exp^{\lambda_3(\tau-\tau_n)} + \lambda_4 C_{5,8} \exp^{\lambda_4(\tau-\tau_n)} - \omega C_6 \sin(\omega\tau + \phi_2), \tag{A.9}$$

where constants are:

$$\lambda_{3,4} = -\xi \pm \sqrt{\xi^2 - 1}, \tag{A.10}$$

$$\tan(\phi_2) = -\frac{2\xi\omega}{1 - \omega^2}, \tag{A.11}$$

$$C_6 = \frac{a}{\sqrt{(1-\omega^2)^2 + (2\xi\omega)^2}}, \tag{A.12}$$

$$C_{4,7} = \frac{\lambda_4(x_n \mp (1-\beta)e) - v_n - C_6[\lambda_4 \cos(\omega\tau_n + \phi_2) + \omega \sin(\omega\tau_n + \phi_2)]}{\lambda_4 - \lambda_3}, \tag{A.13}$$

$$C_{5,8} = \frac{\lambda_3(x_n \mp (1-\beta)e) - v_n - C_6[\lambda_3 \cos(\omega\tau_n + \phi_2) + \omega \sin(\omega\tau_n + \phi_2)]}{\lambda_3 - \lambda_4}. \tag{A.14}$$

Appendix B. Definition of mapping transformations

The six mapping relations illustrated in Fig. 3 are defined as follows.

- *Mapping relation P_{12}:*

$$\begin{pmatrix} e \\ v_2 \\ l_2 \\ m_2 \end{pmatrix} = A_{II}(\tau_{12}) \begin{pmatrix} e \\ v_1 \\ l_1 \\ m_1 \end{pmatrix} + B_{II}(\tau_{12}), \tag{B.1}$$

- *Mapping relation P_{21}:*

$$\begin{pmatrix} e \\ v_1 \\ l_1 \\ m_1 \end{pmatrix} = A_I(\tau_{21}) \begin{pmatrix} e \\ v_2 \\ l_2 \\ m_2 \end{pmatrix} + B_I(\tau_{21}), \tag{B.2}$$

- *Mapping relation P_{23}:*

$$\begin{pmatrix} -e \\ v_3 \\ l_3 \\ m_3 \end{pmatrix} = A_I(\tau_{23}) \begin{pmatrix} e \\ v_2 \\ l_2 \\ m_2 \end{pmatrix} + B_I(\tau_{23}), \tag{B.3}$$

- *Mapping relation P_{43}:*

$$\begin{pmatrix} -e \\ v_3 \\ l_3 \\ m_3 \end{pmatrix} = A_I(\tau_{43}) \begin{pmatrix} -e \\ v_4 \\ l_4 \\ m_4 \end{pmatrix} + B_I(\tau_{43}), \tag{B.4}$$

- *Mapping relation P_{41}:*

$$\begin{pmatrix} e \\ v_1 \\ l_1 \\ m_1 \end{pmatrix} = A_I(\tau_{41}) \begin{pmatrix} -e \\ v_4 \\ l_4 \\ m_4 \end{pmatrix} + B_I(\tau_{41}), \tag{B.5}$$

- *Mapping relation P_{34}:*

$$\begin{pmatrix} -e \\ v_4 \\ l_4 \\ m_4 \end{pmatrix} = A_{III}(\tau_{34}) \begin{pmatrix} -e \\ v_3 \\ l_3 \\ m_3 \end{pmatrix} + B_{III}(\tau_{34}). \tag{B.6}$$

For previous equations matrices are defined depending on the region where the maps are defined.

- *Matrices for region X_I:*

$$A_I(\tau) = \begin{pmatrix} a_{11}(\tau) & a_{12}(\tau) & a_{13}(\tau) & a_{14}(\tau) \\ a_{21}(\tau) & a_{22}(\tau) & a_{23}(\tau) & a_{24}(\tau) \\ 0 & 0 & \cos(\omega\tau) & -\sin(\omega\tau) \\ 0 & 0 & \sin(\omega\tau) & \cos(\omega\tau) \end{pmatrix} \tag{B.7}$$

$$B_I(\tau) = \begin{pmatrix} 0 \\ 0 \\ 0 \\ 0 \end{pmatrix} \tag{B.8}$$

$$\begin{aligned}
a_{11}(\tau) &= \frac{\lambda_2 \exp^{\lambda_1\tau} - \lambda_1 \exp^{\lambda_2\tau}}{\lambda_2 - \lambda_1} \\
a_{12}(\tau) &= \frac{-\exp^{\lambda_1\tau} + \exp^{\lambda_2\tau}}{\lambda_2 - \lambda_1} \\
a_{13}(\tau) &= -C_3[(\lambda_2\cos(\phi_1) + \omega\sin(\phi_1))\frac{\exp^{\lambda_1\tau}}{\lambda_2 - \lambda_1} - (\lambda_1\cos(\phi_1) + \omega\sin(\phi_1))\frac{\exp^{\lambda_2\tau}}{\lambda_2 - \lambda_1} \\
&\quad - \cos(\omega\tau + \phi_1)] \\
a_{14}(\tau) &= -C_3[(-\lambda_2\sin(\phi_1) + \omega\cos(\phi_1))\frac{\exp^{\lambda_1\tau}}{\lambda_2 - \lambda_1} - (-\lambda_1\sin(\phi_1) + \omega\cos(\phi_1))\frac{\exp^{\lambda_2\tau}}{\lambda_2 - \lambda_1} \\
&\quad + \sin(\omega\tau + \phi_1)] \\
a_{21}(\tau) &= \frac{\lambda_1\lambda_2(\exp^{\lambda_1\tau} - \exp^{\lambda_2\tau})}{\lambda_2 - \lambda_1} \\
a_{22}(\tau) &= \frac{-\lambda_1 \exp^{\lambda_1\tau} + \lambda_2 \exp^{\lambda_2\tau}}{\lambda_2 - \lambda_1} \\
a_{23}(\tau) &= -C_3[(\lambda_2\cos(\phi_1) + \omega\sin(\phi_1))\frac{\lambda_1 \exp^{\lambda_1\tau}}{\lambda_2 - \lambda_1} - (\lambda_1\cos(\phi_1) \\
&\quad + \omega\sin(\phi_1))\frac{\lambda_2 \exp^{\lambda_2\tau}}{\lambda_2 - \lambda_1} + \omega\sin(\omega\tau + \phi_1)] \\
a_{24}(\tau) &= -C_3[(-\lambda_2\sin(\phi_1) + \omega\cos(\phi_1))\frac{\lambda_1 \exp^{\lambda_1\tau}}{\lambda_2 - \lambda_1} - (-\lambda_1\sin(\phi_1) \\
&\quad + \omega\cos(\phi_1))\frac{\lambda_2 \exp^{\lambda_2\tau}}{\lambda_2 - \lambda_1} + \omega\cos(\omega\tau + \phi_1)]
\end{aligned} \tag{B.9}$$

- *Matrices for region X_{II} and X_{III}:*

$$A_{II}(\tau) = A_{III}(\tau) = \begin{pmatrix} b_{11}(\tau) & b_{12}(\tau) & b_{13}(\tau) & b_{14}(\tau) \\ b_{21}(\tau) & b_{22}(\tau) & b_{23}(\tau) & b_{24}(\tau) \\ 0 & 0 & \cos(\omega\tau) & -\sin(\omega\tau) \\ 0 & 0 & \sin(\omega\tau) & \cos(\omega\tau) \end{pmatrix} \tag{B.10}$$

$$B_{II}(\tau) = \begin{pmatrix} b_1(\tau) \\ b_2(\tau) \\ 0 \\ 0 \end{pmatrix} \tag{B.11}$$

$$B_{III}(\tau) = \begin{pmatrix} b_3(\tau) \\ b_4(\tau) \\ 0 \\ 0 \end{pmatrix} \tag{B.12}$$

$$\begin{aligned}
b_{11}(\tau) &= \frac{\lambda_4 \exp^{\lambda_3\tau} - \lambda_3 \exp^{\lambda_4\tau}}{\lambda_4 - \lambda_3} \\
b_{12}(\tau) &= \frac{-\exp^{\lambda_3\tau} + \exp^{\lambda_4\tau}}{\lambda_4 - \lambda_3} \\
b_{13}(\tau) &= -C_6[(\lambda_4\cos(\phi_2) + \omega\sin(\phi_2))\frac{\exp^{\lambda_3\tau}}{\lambda_4 - \lambda_3} - (\lambda_3\cos(\phi_2) + \omega\sin(\phi_2))\frac{\exp^{\lambda_4\tau}}{\lambda_4 - \lambda_3} \\
&\quad - \cos(\omega\tau + \phi_2)] \\
b_{14}(\tau) &= -C_6[(-\lambda_4\sin(\phi_2) + \omega\cos(\phi_2))\frac{\exp^{\lambda_3\tau}}{\lambda_4 - \lambda_3} - (-\lambda_3\sin(\phi_2) + \omega\cos(\phi_2))\frac{\exp^{\lambda_4\tau}}{\lambda_4 - \lambda_3} \\
&\quad + \sin(\omega\tau + \phi_2)] \\
b_{21}(\tau) &= \frac{\lambda_3\lambda_4(\exp^{\lambda_3\tau} - \exp^{\lambda_4\tau})}{\lambda_4 - \lambda_3} \\
b_{22}(\tau) &= \frac{-\lambda_3 \exp^{\lambda_3\tau} + \lambda_4 \exp^{\lambda_4\tau}}{\lambda_4 - \lambda_3} \\
b_{23}(\tau) &= -C_6[(\lambda_4\cos(\phi_2) + \omega\sin(\phi_2))\frac{\lambda_3 \exp^{\lambda_3\tau}}{\lambda_4 - \lambda_3} - (\lambda_3\cos(\phi_2) \\
&\quad + \omega\sin(\phi_2))\frac{\lambda_4 \exp^{\lambda_4\tau}}{\lambda_4 - \lambda_3} + \omega\sin(\omega\tau + \phi_2)] \\
b_{24}(\tau) &= -C_6[(-\lambda_4\sin(\phi_2) + \omega\cos(\phi_2))\frac{\lambda_3 \exp^{\lambda_3\tau}}{\lambda_4 - \lambda_3} - (-\lambda_3\sin(\phi_2) \\
&\quad + \omega\cos(\phi_2))\frac{\lambda_4 \exp^{\lambda_4\tau}}{\lambda_4 - \lambda_3} + \omega\cos(\omega\tau + \phi_2)] \\
b_{1,3}(\tau) &= \mp\frac{(1-\beta)e\lambda_4 \exp^{(\lambda_3\tau)}}{\lambda_4 - \lambda_3} \pm \frac{(1-\beta)e\lambda_3 exp^{\lambda_4\tau}}{\lambda_4 - \lambda_3} \pm (1-\beta)e \\
b_{2,4}(\tau) &= \mp\frac{(1-\beta)e\lambda_4\lambda_3 \exp^{(\lambda_3\tau)}}{\lambda_4 - \lambda_3} \pm \frac{(1-\beta)e\lambda_3\lambda_4 exp^{\lambda_4\tau}}{\lambda_4 - \lambda_3}
\end{aligned} \tag{B.13}$$

References

[1] Banerjee S, Verghese GC. Nonlinear phenomena in power electronics: attractors, bifurcations, chaos, and nonlinear control. IEEE Press; 2001.
[2] Theodossiades S, Natsiavas S. Non-linear dynamics of gear-pair systems with periodic stiffness and backlash. J Sound Vib 2000;229:287–310.
[3] Kahraman A, Blankenship GW. Experiments on nonlinear dynamic behavior of an oscillator with clearance and periodically time-varying parameters. J Appl Mech 1997;64:217–26.
[4] Popp K, Stelter P. Stick-slip vibrations and chaos. Philos Trans: Phys Sci Eng 1990;332:89–105.
[5] Galvanetto U. Non-linear dynamics of multiple friction oscillators. Comput Methods Appl Mech Engrg 1999;178(3–4):291–306.
[6] Elbkosh A, Giaouris D, Pickert V, Zahawi B, Banerjee S. Stability analysis and control of bifurcations of parallel connected DC/DC converters using the monodromy matrix. In: 2008 IEEE international symposium on circuits and systems (ISCAS). IEEE; 2008, p. 556–9.
[7] Kahraman A, Singh R. Non-linear dynamics of a spur gear pair. J Sound Vib 1990;142:49–75.
[8] Karagiannis K, Pfeiffer F. Theoretical and experimental investigations of gear-rattling. Nonlinear Dynam 1991;2:367–87.
[9] Sato K, Yamamoto S, Yokota K, Yoshida K, Ohmori T, Aoki T, Karube S. Chaotic behavior in gear system (special issue on nonlinear dynamics). JSME Int J Ser C Mech Syst Mach Elem Manuf 1998;41:577–82.
[10] Goyder HGD, Teh CE. A study of the impact dynamics of loosely supported heat exchanger tubes. J Press Vessel Technol 1989;111:394–401.
[11] Paidoussis MP, Li GX. Cross-flow-induced chaotic vibrations of heat-exchanger tubes impacting on loose supports. J Sound Vib 1992;152:305–26.
[12] Krivtsov AM, Wiercigroch M. Dry friction model of percussive drilling. Meccanica 1999;34:425–34.

[13] Wiercigroch M, Neilson RD, Player MA. Material removal rate prediction for ultrasonic drilling of hard materials using an impact oscillator approach. Phys Lett A 1999;259:91–6.
[14] Farid M. Dynamics of a hybrid vibro-impact oscillator: canonical formalism. Nonlinear Dynam 2021;106(3):1769–87.
[15] Stefani G, De Angelis M, Andreaus U. Numerical study on the response scenarios in a vibro-impact single-degree-of-freedom oscillator with two unilateral dissipative and deformable constraints. Commun Nonlinear Sci Numer Simul 2021;99:105818.
[16] Turki F, Gritli H, Belghith S. Robust position control of a two-sided 1-dof impacting mechanical oscillator subject to an external persistent disturbance by means of a state-feedback controller. Complexity 2019;2019.
[17] Turki F, Gritli H, Belghith S. An LMI-based design of a robust state-feedback control for the master-slave tracking of an impact mechanical oscillator with double-side rigid constraints and subject to bounded-parametric uncertainty. Commun Nonlinear Sci Numer Simul 2020;82:105020.
[18] Lai ZH, Thomson G, Yurchenko D, Val DV, Rodgers E. On energy harvesting from a vibro-impact oscillator with dielectric membranes. Mech Syst Signal Process 2018;107:105–21.
[19] Dai W, Yang J, Shi B. Vibration transmission and power flow in impact oscillators with linear and nonlinear constraints. Int J Mech Sci 2020;168:105234.
[20] Ouakad HM, Al-Harthi M, Bahadur IB. On the use of nonlinear impact oscillators in vibrating electromagnetic based energy harvesters. J Intell Mater Syst Struct 2021;1654–62.
[21] Wiercigroch M, Kovacs S, Zhong S, Costa D, Vaziri V, Kapitaniak M, Pavlovskaia E. Versatile mass excited impact oscillator. Nonlinear Dynam 2020;99(1):323–39.
[22] Pasternak E, Dyskin A, Qi C. Shifted impact oscillator: Tuned multiple resonances and step load. Internat J Engrg Sci 2020;147:103203.
[23] Makarenkov O, Verhulst F. Resonant periodic solutions in regularized impact oscillator. J Math Anal Appl 2021;499(2):125035.
[24] Paidoussis MP. A review of flow-induced vibrations in reactors and reactor components. Nucl Eng Des 1983;74:31–60.
[25] Weaver DST, Fitzpatrick JA. A review of cross-flow induced vibrations in heat exchanger tube arrays. J Fluids Struct 1988;2:73–93.
[26] Pettigrew MJ, Carlucci LN, Taylor CE, Fisher NJ. Flow-induced vibration and related technologies in nuclear components. Nucl Eng Des 1991;131:81–100.
[27] Piteau P, Delaune X, Antunes J, Borsoi L. Experiments and computations of a loosely supported tube in a rigid bundle subjected to single-phase flow. J Fluids Struct 2012;28:56–71.
[28] Christon MA, Lu R, Bakosi J, Nadiga BT, Karoutas Z, Berndt M. Large-eddy simulation, fuel rod vibration and grid-to-rod fretting in pressurized water reactors. J Comput Phys 2016;322:142–61.
[29] Natsiavas S. Stability and bifurcation analysis for oscillators with motion limiting constraints. J Sound Vib 1990;141:97–102.
[30] Foale S. Analytical determination of bifurcations in an impact oscillator. Philos Trans R Soc Lond Ser A: Phys Eng Sci 1994;347:353–64.
[31] Chin W, Ott E, Nusse HE, Grebogi C. Grazing bifurcations in impact oscillators. Phys Rev E 1994;50:4427.
[32] Nordmark AB. Non-periodic motion caused by grazing incidence in an impact oscillator. J Sound Vib 1991;145:279–97.
[33] Li GX, Rand RH, Moon FC. Bifurcations and chaos in a forced zero-stiffness impact oscillator. Int J Non-Linear Mech 1990;25:417–32.
[34] Kleczka M, Kreuzer E, Wilmers C. Crises in mechanical systems. In: Nonlinear dynamics in engineering systems. Springer; 1990, p. 141–8.
[35] Wiercigroch M. Bifurcation analysis of harmonically excited linear oscillator with clearance. Chaos Solitons Fractals 1994;4:297–303.
[36] Wiercigroch M, Sin VWT. Experimental study of a symmetrical piecewise base-excited oscillator. J Appl Mech 1998;65:657–63.
[37] Luo ACJ, Menon S. Global chaos in a periodically forced, linear system with a dead-zone restoring force. Chaos Solitons Fractals 2004;19:1189–99.
[38] Luo ACJ. The mapping dynamics of periodic motions for a three-piecewise linear system under a periodic excitation. J Sound Vib 2005;283:723–48.
[39] Luo ACJ. Singularity and dynamics on discontinuous vector fields. Elsevier; 2006.
[40] Luo ACJ, Guo Y. Vibro-impact dynamics. John Wiley & Sons 2012.
[41] Luo ACJ, O'Connor DM. System dynamics with interaction discontinuity. Springer 2015.
[42] Natsiavas S. Periodic response and stability of oscillators with symmetric trilinear restoring force. J Sound Vib 1989;134:315–31.
[43] Chong ASE, Yue Y, Pavlovskaia E, Wiercigroch M. Global dynamics of a harmonically excited oscillator with a play: Numerical studies. Int J Non-Linear Mech 2017;94:98–108.
[44] Foale S, Bishop SR. Bifurcations in impact oscillations. Nonlinear Dynam 1994;6:285–99.
[45] Ing J, Pavlovskaia E, Wiercigroch M, Banerjee S. Experimental study of impact oscillator with one-sided elastic constraint. Phil Trans R Soc A 2008;366:679–705.
[46] Ing J, Pavlovskaia E, Wiercigroch M, Banerjee S. Bifurcation analysis of an impact oscillator with a one-sided elastic constraint near grazing. Physica D 2010;239:312–21.
[47] Mason JF, Piiroinen PT. Saddle-point solutions and grazing bifurcations in an impacting system. Chaos 2012;22:013106.
[48] Jiang H, Wiercigroch M. Geometrical insight into non-smooth bifurcations of a soft impact oscillator. IMA J Appl Math 2016;81:662–78.
[49] Molenaar J, de Weger JG, van de Water W. Mappings of grazing-impact oscillators. Nonlinearity 2001;14:301.
[50] Di Bernardo M, Feigin MI, Hogan SJ, Homer ME. Local analysis of C-bifurcations in n-dimensional piecewise-smooth dynamical systems. Chaos Solitons Fractals: Interdiscip J Nonlinear Sci Nonequilibrium Complex Phenom 1999;11:1881–908.
[51] Feigin MI. Doubling of the oscillation period with C-bifurcations in piecewise-continuous systems. J Appl Math Mech 1970;34(5):822–30.
[52] Feigin M. On the structure of C-bifurcation boundaries of piecewise-continuous systems. J Appl Math Mech 1978;42(5):885–95.
[53] Nusse HE, Yorke JA. Border-collision bifurcations including "period two to period three" for piecewise smooth systems. Physica D 1992;57(1–2):39–57.
[54] Di Bernardo M, Budd C, Champneys AR, Kowalczyk P. Piecewise-smooth dynamical systems: theory and applications, Vol. 163. Springer Science & Business Media; 2008.
[55] Jiang H, Chong ASE, Ueda Y, Wiercigroch M. Grazing-induced bifurcations in impact oscillators with elastic and rigid constraints. Int J Mech Sci 2017;127:204–14.
[56] Chong A. Numerical modelling and stability analysis of non-smooth dynamical systems vie ABESPOL (Ph.D. thesis), University of Aberdeen; 2016.